Submitted: 18 August 2023

Published online in 'accepted manuscript' format: 04 April 2024

Manuscript title: A microstructural insight into the compression behaviour of scaly clays

Authors: Matteo Pedrotti*, Alessandro Tarantino*, Antonio Annese†, Federica Cotecchia‡ and Claudia Vitone‡

Affiliations: *Department of Civil and Environmental Engineering, University of Strathclyde, Glasgow, UK; †CASTIGLIA SRL, Massafra, Italy and ‡Department of Civil, Environmental, Land, Construction and Chemistry (DICATECh), Politecnico di Bari, Italy

Corresponding author: Matteo Pedrotti, Department of Civil and Environmental Engineering, University of Strathclyde, James Weir Building - Level 5, 75 Montrose Street - Glasgow G1 1XJ, Scotland, UK.

E-mail: matteo.pedrotti@strath.ac.uk

Abstract

Scaly clays are intensely fissured clays with lens shaped elements of millimetre size and show a complex compression behaviour that poses challenges to the design and construction of geostructures (excavations, retaining diaphragms, and tunnels). Scaly clays show a Normal Compression Line (NCL) where plastic deformation accumulates as typically observed in non-scaly clays. Yet the response observed upon unloading and subsequent reloading is very peculiar, i) the unloading-reloading cycle is typically a close-loop with relatively large hysteresis; ii) the compressibility recorded at high OCR ratio of the unloading or reloading branches is close to the NCL compressibility. This paper presents a microstructural study on an Italian scaly clay where SEM observations are integrated with Mercury Intrusion Porosimetry (MIP) analyses and X-ray Computed Tomography (XCT) images. The mechanism associated with the closing of inter-*scale* porosity and the generation of new intra-*scale* porosity was identified as the process responsible for the plastic deformation. Experimental observation of reconstituted clay showed a "quasi-reversible" behaviour upon loading and unloading and a pore size distribution characterized only by interparticle porosity. The observation that unloading and reloading curves are parallel in natural and reconstituted clays, led to postulate that the interparticle porosity is controlling the elastic response.

Introduction

Natural clays may develop complex structures during their geological history. This is the case of clays located within chain areas; the more ancient and complex is their geological history, the more intensely fissured is the clay (Skempton, 1969; Chandler, 1973). An intensely fissured clay exhibits relatively low shear strength, markedly lower than the same clay in reconstituted state (Vitone and Cotecchia, 2011, Vitone et al., 2013, Nardelli et al., 2016). As a result, slope instabilities are often observed in intensely fissured clays (Pechalat et al., 1979, Fearon and Coop, 2002, Santaloia et al., 2001, Silvestri et al., 2007, Gens, 2013). Moreover, their well-known very high swelling capacity poses several problems in tunnel lining (e.g., Bilotta et al. (1985) and Cotecchia and Valentini (1973)). Owing to the presence of fissures, the coupling between shear strength and volumetric behaviour follows relatively complex pattern.

The intensely fissured clay investigated here is the one from Santa Croce di Magliano in Italy (SCM, thereafter), i.e., the same as that studied by Vitone and Cotecchia (2011). This clay is known as 'scaly clay' for being crossed by fissures splitting the clay into millimetre-sized *scales*. Vitone and Cotecchia (2011) showed that, as often the case for intensely fissured clays, also the SCM clay is much less compressible than the same clay in reconstituted state. The compression curves of natural and reconstituted SCM scaly clay are shown in Figure 1, compared to the Intrinsic Compression Line (ICL, hereafter) defined by Burland (1990) and to other two highly fissured natural clays both investigated in Vitone and Cotecchia (2011). Following Burland (1990), the void ratio e is normalised with respect to the void ratios e^*_{100} and e^*_{1000} of the reconstituted clay at 100kPa and 1000 kPa vertical effective stress respectively. For the natural clay, i) the slope of the loading curve departing from the in-situ stress state and the slope of the subsequent unloading curve appear to be very similar and ii) such slope is also similar to the slope of the unloading curve of the same clay in reconstituted state (as shown in Figure 1 after Vitone and Cotecchia, 2011). Such observations may lead to the conclusion that the natural soil is in an overconsolidated state.

This apparent overconsolidation should lead to a '*dry*' response (Schofield and Wroth, 1968) in undrained shearing, i.e., triaxial samples would be expected to reach their ultimate deviator stress by increasing their mean effective stress. However, experimental observations show a more complex and, to some extent, unexpected pattern.

Samples of the SCM scaly clay investigated by Vitone and Cotecchia (2011) loaded from the in-situ effective stress showed a '*wet*' undrained behaviour (mean effective stress decreased upon undrained shearing) whereas samples on the unloading curve following the first loading showed a '*dry*' undrained behaviour (mean effective stress increased upon undrained shearing). Within the classical framework of critical state soil mechanics where hardening is controlled by the (total) specific volume, this pattern would suggest that the natural soil at the in-situ stress state was normally consolidated. As such, one would expect that the clay exhibited a 'dry' behaviour upon reloading (since OCR>1). Upon reloading, samples showed instead a wet behaviour. A possible explanation for this puzzling behaviour is that the hardening is not controlled by the total specific volume but some specific class of pores (scaly clays show multi-scale porosity visible even to the naked eye). For example, if the plastic behaviour is controlled by the interaction between the *scales*, it would be the inter-*scale* specific volume that would control the hardening and not the total specific volume. This hypothesis is explored further in this paper.

It is also worth observing that the loading-unloading curves of the natural SCM scaly clay (in red in Figure 1), which is rich in smectite, seem to generate a closed-loop as often observed in reconstituted smectite clays (*Reconstituted Montmorillonite – Shridaran 1973* and *Reconstituted – Di Maio 1996* in Figure 1). However, the loading-unloading loop of the natural SCM scaly clay appears to be relatively narrow compared to the one in reconstitute state. This again may suggest that the compression behaviour of the scaly clay is controlled by specific sub-classes of pores rather than the total porosity as generally occurs in unfissured (intact) clays.

This paper addresses three research questions related to the compression behaviour of the SCM scaly clay, i) what are the classes of pores involved in its volumetric response; ii) what is their evolution upon loading from the in-situ- stress state and subsequent unloading; iii) why the slope of the loading-unloading curve of the natural clay is very similar to the slope of the unloading curve of the same clay in reconstituted state. These questions would cast light on the different *dry/wet* response of the scaly clay in undrained shear.

To investigate the scaly clay microstructure, the pore-size distribution of natural and reconstituted scaly clay samples taken along loading/unloading paths was investigated across extended pore-size range via unique integration of Mercury Intrusion Porosimetry (MIP) and X-ray Computed Tomography (XCT) data. Pore-size distribution data were then complemented by qualitative analysis of Scanning Electron Microscope (SEM) images.

Material

Following the experimental campaign published in Vitone and Cotecchia (2011), new sampling campaigns were carried out in winter 2016 and 2021 in the same site. The scaly clay has been sampled down in Santa Croce di Magliano, a small town at high landslide risk (Cotecchia et al., 2015) in the southern Italian Apennines. The samples were extracted from an outcropping in the SCM territory at 3-6 meters below ground level, after removal of a thick stratum of soil. The samplers were pushed directly into the soil soon after lubricating their inner surface with silicon oil to minimise friction. Due to the geological history, characterised by large deformations induced by tectonic processes, an intense network of fissures splits the clay into millimetre-sized lens-shaped elements (known as *scales*—which is the origin of their being referred to as scaly clays in the literature). Each *scale* can be in turn characterized by a '*scale*-in-*scale*' fabric, of millimetre size in both length and thickness (Figure 2).

The intense fissuring network of the SCM scaly clay is due to the tectonic processes experienced by the clay during its geological history since the Oligocene–Miocene as part of a succession of clayey and calcareous strata (i.e. Undifferentiated Clayey Complex by Melidoro et al. (2002)). As reported in Table 1 the fissuring intensity is the highest possible (I6: very high) in the F-ID chart proposed by Vitone and Cotecchia (2011), due to both the small average volume of the *scales* (about 0.15 cm^3) and their very high specific surface (about 1000 m^2/m^3). At the scale of a laboratory specimen, there is mainly *one single* prevailing direction of the *scales*, which coincides with the orientation of the fissures (F1 in the F-ID chart). SCM clay is a silty clay (clay fraction: CF = 83%; silt fraction: MF= 16%) of high plasticity (PI= 0.59) for its high liquid limit (w_L=99%), and it can be classified as CH according to the USCS (ASTM D2487). The X-ray diffraction analyses confirm that the high activity of the SCM scaly clay (A = 0.7) results from large quantities of smectite and mixed illite-smectite layers (Table 1)

Experimental procedures and testing programme

Oedometer Tests

A new set of one-dimensional compression tests were carried out at the Politecnico di Bari. The mechanical behaviour of the scaly clay was compared with that of the same clay when reconstituted in the laboratory, following Burland (1990). Fearon and Coop (2002) have shown that, even for scaly clays, standard reconstitution generates a material representative of an unfissured structure as for any other reconstituted clay, despite the presence of relicts of *scales* in the reconstituted material.

The oedometer specimens of natural scaly clay have been prepared by setting fissures always normally to the direction of the axial stress. The oedometer step-loading tests were carried out with double-end drainage on 50 mm diameter and 19 mm high specimens (ASTM, 2011), which have been shown to include representative patterns of fissures for clays of fissuring intensity I6 (Vitone and Cotecchia (2011), Vitone et al. (2013a, 2013b)). To prevent destructuration, care was taken to avoid that after submersion in the oedeometer cell, the natural scaly clay specimens did not exhibit significant swelling. To this end, the vertical stress was varied intermittently to maintain a quasi-constant height during the process of equalisation of the pore-water pressure against the (zero) water pressure in the external container of the oedometer cell. The vertical stress required to maintain constant volume at the end of the pore-water pressure equalisation process was ~400 kPa. In the subsequent loading steps, primary consolidation was assumed to be completed when the displacement rate attained 0·01–0·02 mm/d. Different 1D hydro-mechanical loading paths were imposed on 5 specimens as detailed in the following(OED1 to OED5).

The five specimens tested at the Politecnico di Bari (OED1 to OED5) were preserved and sent to the University of Strathclyde for micro-structural investigation as illustrated in Figure 3a and Table 2. ¼ of each specimen was scanned with the X-CT, other two quarters of the specimen prepared for SEM and MIP test respectively as described below and the remaining quarter used to measure the water content.

OED4 is the specimen allowed to equilibrate with the external water under quasi-constant volume and represents the in-situ condition. The other specimens were first equilibrated as per specimen OED4 and then loaded to either 1200kPa or 6400 kPa (OED5 and OED1 respectively), loaded to 6400 kPa and unloaded to 400 kPa (OED3) or directly unloaded from the in-situ stress state to 50kPa (OED2).

The reconstituted material for 1D tests was prepared following the standard preparation procedure: the natural soil was broken into small pieces, exposed to tap water to bring it to a water content 1.5 times the liquid limit, and let to swell overnight in a watertight bag. The soil was then remoulded by hand-mixing and again left to hydrate overnight before the liquid limit test was carried out. The water content of the slurry was reduced by compression in a consolidometer to a value at which the Atterberg limits could be measured, or the sample could be handled to put it in the oedometer apparatus. Two oedometer tests were carried out on reconstituted specimens. In test OED1*, the specimen was loaded to 6400 kPa under drained conditions and unloaded rapidly under undrained condition. In test OED2*, the specimen was loaded to 4900 kPa under drained conditions and unloaded still under drained conditions.

No microstructural investigation was carried out on reconstituted specimen OED1* and OED2*.

Preparation of natural and reconstituted clay samples along isotropic paths for microstructural investigation

Isotropic compression tests where suction was increased by specimens air-drying were performed at the University of Strathclyde on both natural clay samples and sample reconstituted from slurry (Figure 3b). As the samples dried, the water loss, the suction and total volume were measured. Water loss was measured with a 0.1 mg precision scale, whereas suction was measured by means of WP4C Dewpoint potential meter. Drying was carried out to different target water contents. At the end of the drying tests, part of each sample was oven-dried at 105 °C for 24 hours and weighed. As water content and dry mass were measured, the void ratio could be back calculated for each drying step.

Specimens remained saturated up to a suction of ~800 kPa and then desaturated. The dashed curve in Figure 3b shows qualitatively the change in void ratio that would have been recorded under any suction for natural and reconstitutes samples (black and orange respectively). The specimens Recon-s400 and *N* remained saturated whereas the specimens Recon-s1400, Recon-s2800, and N-s9000 were brought to an unsaturated state.

The reconstituted specimens were compressed isotropically via increasing suction instead of being compressed mechanically under 1D conditions in the oedometer because oedometers were temporarily out of service at the University of Strathclyde at the time of the experimental campaign. It is shown later in the paper that the microstructure of saturated reconstituted specimens compressed isotopically via suction can be considered representative of reconstituted specimens if compressed mechanically in the oedometer under 1D conditions.

Microstructural investigation

Mercury Intrusion Porosimeter

Clay pore size distribution was measured at the University of Strathclyde by means of Mercury Intrusion Porosimetry (MIP), using a Quantachrome Instrument Poremaster 60. The pore-size is measured in the range 0.003-1000 μm, corresponding to 1.5 to 420000 kPa of mercury intrusion pressure. Data were interpreted by assuming a contact angle between mercury and clay particles of 147° and a mercury surface tension of 0.484 N/m (Diamond, 1970). Blank tests and mercury intrusion rate were chosen in order to minimize error associated with temperature and system compressibility as described in Pedrotti (2016), Pedrotti and Tarantino (2018). Each specimen was dehydrated via freeze-drying by rapidly submerging the clay sample in an isopentane bath at its melting point -159°C, in turn reached by means of liquid nitrogen (Pedrotti, 2016). Once the isopentane was at its melting point, clay specimens were rapidly plunged in the isopentane slush.

MIP data were interpreted by assuming that the single pore is characterised by two parallel plates and that the plate distance is small compared to the plate dimension. Under this assumption, the air-water interface turns into a cylindrical surface and the Young-Laplace equation can be written as:

$$P = -\frac{2 \cdot \gamma \cdot cos\theta}{D} \qquad [1]$$

where P is the mercury intrusion pressure [Pa], γ [N/m] is the mercury surface tension, θ [°] is the clay-mercury contact angle, and D [m] is the pore diameter.

As the volume of the solids fraction was measured for each pressure, the associated intruded porosity could be calculated. The frequency distribution was calculated by deriving the cumulative distribution by finite differences. Finite difference diameter values were chosen to be equally spaced on a logarithmic scale. To reduce the scatter of the frequency distribution,

the logarithm of two subsequent diameters, $log(d_i/d_{i-1})$, was chosen to be 0.159. The frequency distribution was calculated by using the custom-made Python package (https://github.com/PedroMat8/micropy 10.5281/zenodo.3524929). MIP data are presented in terms of MIP void ratio e_{MIP} (volume of mercury intruded per volume of solids) when reporting the cumulative pore-size distribution to enable the comparison between the MIP void ratio and the void ration determined macroscopically in a traditional way. The pore-size frequency distribution is presented in terms of volume intruded by mercury normalised to the total pore-volume to facilitate the comparison between natural and reconstituted specimens (characterise by a very different macroscopic void ratio). Specimens tested in the MIP are reported in Table 2.

X-ray computed tomography

X-ray computed tomography (X-CT) was performed on different clay specimens at the University of Strathclyde by means of Nikon XT H 320 X-ray computed tomography system. 3141 projections per sample were acquired at energy of 141 kV, current of 59-64 μA, resulting in a voxel size of about 20 μm. Clay specimen dimensions where ¼ of the oedometer samples. During each scan the clay specimens were covered with Parafilm ™ to limit water evaporation. For each tomography the reconstruction was performed with Nikon' software CT Pro 3D. The software FIJI (Schindelin et al., 2012) was used for the post-imaging analysis. For all images, a 3D Gaussian blur filter (standard deviation 2) and a Kuwahara filter (sampling window of 5) were applied.

The analysis of the voids volume from the X-ray tomography was performed by means of a 3D discretization in different classes of the pore space by using the FIJI plugin *Beat,* as described in Münch and Holzer (2008). The 3D volume was segmented into the solid and the void space. A global threshold algorithm (Maximum Entropy https://imagej.net/plugins/maximum-entropy-threshold) was used. On the segmented 3D image, the phase associated with the pore space was divided in a given number of subregions and a 3D "distance map" indicating the distance of each pixel to the closest boundary was created (Figure 4). By selecting the contour lines, the required diameter classes were then isolated, and the associated volume was calculated. Such a methodology was preferred with respect to the simpler widely adopted approach where the size of each pore is calculated as the diameter of the sphere having the equivalent volume (Münch and Holzer, 2008). Once the

cumulative distribution of the porosity was derived, the frequency distribution was calculated following the approach adopted for the MIP data. Specimens scanned by X-CT are reported in Table 2.

Merging MIP and XCT data

The pore-size distribution data derived from MIP and XCT image analysis overlapped in the pore-size range 88-173 μm and needed to be realigned. The cumulative pore-size distribution derived from the XCT images was shifted by a value Δ as shown in Figure 5. Δ was calculated via Least Square Optimisation within the overlapping range to best fit the final part of the cumulative curve measure via MIP.
Once that a merged cumulative porosity distribution was created, a new frequency distribution was computed as described above.

By matching the two techniques, one could assume that any undetected pore volume belongs only to pores smaller than 3nm (lower detection limit of MIP). Accordingly, the amount of pores with such dimension was subsequently quantified as arithmetic difference between the pore volume detected by MIP and XCT and the pore volume measured macroscopically (i.e. void ratio).

Scanning Electron Microscope Imaging

Selected samples of scaly clay were imaged by means of Field Emission Scanning Electron Microscope (FE-SEM) (Hitachi SU-6600) at the University of Strathclyde. Images were acquired with a magnitude factor of x90, x1.30k, 3.00k and 6.00k and a beam energy of 10kV. SEM samples were dehydrated by freeze-drying as described above.

Results

Macroscopic behaviour of natural and reconstituted samples

1D loading and unloading

Figure 6 shows the results of the oedometer tests on natural and reconstituted samples of the SCM scaly clay. The compression curves of the natural samples lie on the left of the normal compression line of the corresponding reconstituted sample (i.e. the Intrinsic Compression Line, ICL; Burland (1990)), as already found for other scaly clays by Vitone and Cotecchia (2011). Moreover, these data give evidence that, at high pressures (σ'_v = 6400 kPa), the compression lines of the natural and the reconstituted clays tend to converge. The arrow in

Figure 6 indicates the stress-state range of the gross yield of the scaly clay under study. As observed for many other fissured clays (Cicolella and Picarelli, 1990, Picarelli et al., 2003, Santaloia et al., 2001, Cotecchia and Vitone, 2011), scaly clays do not show an abrupt stiffness reduction at any point.

The results in Figure 6 extend the framework presented in Vitone and Cotecchia (2011) up to large vertical effective stress values (σ'_{vmax} = 6400 kPa): unlike natural unfissured clays, the Normal Compression Line (NCL) of the natural fissured clay does not enter the 'structure-permitted' space (Leroueil and Vaughan, 1990) on the right of the ICL but is located on the left of the ICL. At such high pressures, the NCL of the clay under study converges to the ICL (associated with the scaly clay in reconstituted state).

Suction-induced loading

Suction-induced compression data for natural specimens (N) and specimens reconstituted from slurry (Recon) are compared in Figure 7 to the 1D compression data of the specimen reconstituted from slurry (OED1*), and natural specimens (OED4, OED5 and OED1 in Figure 6). To enable the comparison, all data are plotted in terms of void ratio and mean effective stress p'. The mean effective stress for the oedometer tests was computed by considering a friction angle ϕ' at the critical state of 11.5° and 18° for the sample reconstituted from slurry and the samples consolidated from the natural state respectively, as reported in Vitone and Cotecchia (2011) and assuming the earth coefficient at rest to be equal to $k_0 = 1\text{-}\sin\phi'$. For the suction-induced compression, the void ratio was plotted against suction s. The isotropic path obtained by air-drying and 1D compression are equivalent in the sense that compression generated by an increase in total stress (at zero pore-water pressure) as occurs in an oedometer test is equivalent to the compression generated by increasing suction (at zero total stress) under saturated conditions provided the oedometer test is interpreted in terms of isotropic effective stress (Tarantino et al., 2010).

In the saturated range (specimens *N* and Recon-s400), S_r=1 and suction coincides with the isotropic effective stress. It is remarkable that the data point *N* (suction and void ratio measured on the natural sample) and the data point OED4 (associated with the vertical effective stress required to maintain constant volume of the specimen in the oedometer after sample submersion) are overlapping. The data point recon-s400 associated with the reconstituted clay loaded isotopically to s=400 kPa also appears to lie on the curve derived

from oedometer compression of the reconstituted scaly clay (OED1*). As such, the state achieved by natural and reconstituted clays due to suction induced isotropic compression can be considered equivalent to the state achieved by oedometer compression.

At higher suction (s=2800 kPa), the degree of saturation is lower than unity (air-entry for both natural and reconstituted clay occurs in the suction range 800-4000 kPa) and the void ratio tends to level off at values higher than the corresponding void ratio on the oedometer compression curve as usually observed in clays Tar and Ferreira, 1998, Tar et al., 1999, Vesga, 2009). The void ratio at high suction can be assumed to be very close to the void ratio on the saturated isotropic compression curve at the air-entry suction (Tarantino et al., 2010, Murray and Tarantino, 2019).

Pore space evolution

1D loading and unloading of natural samples

The cumulative pore size distribution of the natural scaly clay specimens subjected to one dimensional loading or unloading (Figure 6) is shown in Figure 8. The void ratio probed by the MIP and XCT is compared to the void ratio measured macroscopically (horizontal lines in Figure 8). The amount of void space not captured by the microstructural analysis increases with the maximum vertical effective stress along the loading path from the in-situ stress state, with the void ratio discrepancy being ~0.20 (22.8%) for specimen OED4 (400 kPa), 0.23 (29.7 %) for OED5 (1200 kPa), and 0.33 (54.6%) for OED1 (6400 kPa). The discrepancy remains high when unloading from the maximum applied stress ~0.3 (37%) for OED3 (400 kPa). Only the sample directly unloaded from the in-situ stress state appears to show little discrepancy being ~0.05 (5%) for OED2 (50 kPa).

It is assumed that the gap between the volume probed by MIP + XCT and the pore volume measured macroscopically is associated with the smaller pores (<0.03 μm) and not with the larger pores (>1000 μm). The cumulative pore-size distribution shows indeed zero gradient at the largest pore-size (1000 μm) and gradients greater than zero at the smallest pore size (0.03 μm).

The frequency pore-size distributions (Figure 9) all exhibit three modal values, associated with pore classes referred to as P1, P2, and P3 (shaded in Figure 9). The percentage of the volume of voids associated with each class is also shown in Figure 9.

The evolution of the pore-size distribution from the in-situ stress state at ~400 kPa (OED4) to gross yielding at 1200 kPa (OED5) and post-yielding normal compression to 6400 kPa (OED1) can be analysed by comparing Figure 9b to Figure 9d.

The class P1 porosity increases slightly from 400 kPa to 1200 kPa (OED4 to OED5) and substantially at 6400 kPa following gross yielding (OED5 to OED1). The class P2 porosity remains almost unchanged from 400 kPa to gross yielding at 1200 kPa but disappears almost entirely at 6400 kPa post-yield stress. The class P3 porosity markedly decreases up to gross yielding at 1200 kPa and slightly decreases after yielding (from 46% to 29% to 22% respectively).

The modal value for class P1 appears to remain essentially constant (~20nm) throughout the loading process. The modal value for class P2 reduces slightly from 0.6 μm to 0.3 μm when stress is increased from 400 kPa to gross yielding at 1200 kPa. The modal value of class P3 appears less defined and more difficult to characterise.

The evolution of the pore-size distribution upon unloading from the in-situ stress state at ~400 kPa (OED4) to 50 kPa (OED2) can be analysed by comparing Figure 9b with Figure 9a. The class P1 porosity decreases (from 36% to 23%), the class P2 increases (from 19% to 34%), and the class P3 appears to remain essentially unchanged (from 46% to 42%). It is worth noting that P1 porosity reduces almost the same amount by which P2 porosity increases. Upon unloading from the in-situ stress state, the modal pore-size associated with P1 and P3 classes remains unchanged, whereas the modal pore-size associated with the class P2 rebounds from 0.6 μm to 0.9 μm.

When the clay is unloaded from 6400 kPa post-yield stress (OED1, Figure 9d) to 400 kPa (OED3, Figure 9e), P1 and P2 porosities show similar pattern, i.e., P1 porosity reduces almost the same amount by which P2 porosity increases. The P3 pores also increases from 22% to 31%.

In both unloading processes, i.e., from the in-situ stress state (OED4 to OED2) and from post yield stress (OED1 to OED3), the pore class P2 appears to be the one that dominates the rebound upon unloading.

The full loading and unloading cycle from 400 kPa to 6400 kPa and back to 400 kPa can be analysed by comparing the pore-size distributions of specimens OED4 and OED3 (Figure 9b and Figure 9e, respectively). After yielding, the class P1 porosity appear to increase mainly at the expenses of the reduction of class P3 porosity. The class P2 porosity remains essentially unchanged (slightly reduces from 19% to 14%) and so does the P2 modal pore-size (~0.6 μm).

Isotropic loading on natural and reconstituted specimens

The pore-size distribution of the saturated natural samples after sampling and under the in situ-stress state in the oedometer (N and OED4 respectively), and the saturated reconstituted sample loaded via increasing suction to same isotropic effective stress as in the field (Recon=s400) are presented in Figure 10 (macroscopic data presented in Figure 7). Only data from MIP analyses are reported for the natural and reconstituted sample subjected to suction-induced isotropic confining stress as no X-CT was performed on these samples. As expected, the two natural samples have similar pore-size distribution being subjected to the same effective stress. The pore-classes P1, P2, and P3 are all present. On the other hand, the saturated reconstituted sample only shows pores in the class P2.

The cumulative pore-size distributions are compared in Figure 10b where the macroscopic void ratio is also shown as a reference. All the pores of the reconstituted sample are intruded by mercury, e.g., the class P2 represents to totality of the pore-volume. The natural samples show a gap between the macroscopic void ratio and the void ratio probed by MIP (sample N) or the MIP +XCT (sample OED4). As discussed earlier, this gap is attributed to the smaller pores not intruded by mercury, which are present in the natural samples but not in the reconstituted ones.

The pore-size distribution of natural and reconstituted samples compressed by either increasing the vertical stress in the oedometer (OED1) or increasing suction to high values (N-s9000 and Recon-s2800) are shown in Figure 11a. The intermediate pore class P2 in the natural samples disappears, regardless of whether the sample is compressed by increasing vertical stress in the oedoemeter or by increasing suction. This is not the case for the reconstituted sample where the class P2 persists even at high suction.

The cumulative pore distribution (Figure 11b) confirms that all pores are intruded by mercury in the reconstituted samples as opposed to the natural samples where the smaller pores are not probed by MIP (as inferred by the gap between the macroscopic void ratio and the void ratio associated with either MIP (N-s9000) or MIP+XCT (OED1).

Evolution of pore classes

To quantify the evolution of each pore class, the partial void ratio of each pore-class was calculated by separating the three pore classes via the position of the valleys in the PSD distribution as shown in Figure 12. The missing volume of voids (i.e., the difference between the volume of voids measured macroscopically and volume of voids inferred from MIP + XCT) was assumed to belong to the P1 class of pores.

The evolution of the macroscopic and the partial void ratios with vertical stress along the loading-unloading path from the in-situ stress state and the direct unloading from the in-situ stress state are shown Figure 13. The following observations can be made:

i. A full loading-unloading cycle from the in-situ stress state causes an irreversible reduction of the porosity P3, which is approximately equal to the increase in porosity P1, i.e., plastic deformation is associated with permanent reduction of porosity P3 'poured' into porosity P1.
ii. Porosity P2 vanishes upon loading to the maximum vertical stress and bounces back quasi-elastically to its initial value upon unloading.
iii. Unloading from the initially overconsolidated in-situ stress state generates new porosity P2 and partially counterbalanced by reduction in porosity P1; porosity P3 remains constant.
iv. Unloading from normally consolidated state (6800 kPa) generates slight increase of porosities P3 partially compensated by a decrease in porosity P1.

SEM – Particle configuration

SEM images at different magnitudes for the 5 samples tested in the oedometer are compared in Figure 14. Figure 14a and Figure 14b compare the particle configuration of sample in its natural state after sampling (N) with that of the sample maintained at constant volume after submersion in the oedometer cell (OED4). Throughout the different magnifications, the two samples show similar particle configuration. Polygonal *scales* of parallel and oriented particles are visible (shaded area in Figure 14a2 and Figure 14b1). Elongated and oriented fissures of different dimensions (Figure 14a2 and Figure 14b2) run along the *scale*'s edges.

The increased magnification also allows focusing within the *scales* (rows *c* and *d* in Figure 14). It can be observed that *scales* are made of arrays of parallel particles (wavily sheets in row 3 and 4 of columns N and OED4). Fissures between *scales*, *scales* and particles inside the *scales* appear to have the same sub-horizontal orientation. Between the arrays of parallel particles, another class of oriented and elongated pores can be discerned although not readily visible. Such class of elongated smaller pores, appear to have dimensions of the same order of magnitude of the particle thickness.

Column OED1 in Figure 14 shows the particle configuration of the specimen loaded in the oedometer to 6400 kPa. *Scales*, fissures, and intra-*scale* particle configuration appear to follow the same pattern observed for samples N and OED4. However, inter-*scale* fissures seem narrower and less persistent. Only two pore classes are clearly visible in these images: the pores between the densely packed parallel particles within the *scales* and the fissures surrounding the *scales*. These two classes are associated with the pore classes P1 and P3 showed in Figure 9.

Column OED2 in Figure 14 shows the particle configuration upon 1D unloading from in-situ stress state. The sample fabric appears to be different from the three samples examined so far (natural state after sampling, in-situ stress state in the oedometer, and loading to the maximum vertical stress of 6800 kPa). Fissures are still visible but in a less persistent fashion. Arrays of oriented particles are still visible but particles appear to be swollen "swollen particles" in Figure 14d4), causing the pore space between particles to be more rounded and less oriented. This finding seems to agree with the observation that the volume of the pore class P2 increases when the clay is unloaded from the in-situ stress state (Figure 12d).

The particle configuration of sample Recon-s2800, i.e. reconstituted from slurry and subjected to suction-induced compression up to a suction of about 2800 kPa, is shown in column 'Recon-s2800' in Figure 14. Inter-*scale* fissures are not visible and this appears to agree with the very small pore-volume in class P3 observed in the PSD of sample 'Recon-s2800' (Figure 11).

CONCEPTUAL MODEL FOR THE MICROSTRUCTURE

Based on the pore-size distribution inferred from combined MIP and XCT and the observation of SEM images, a conceptual model for the microstructure of scaly clays in natural and reconstituted state and their evolution upon loading and unloading are put forwards in Figure 15 and Figure 16. Each figure specifically address i) which are the classes of pores involved in the volumetric response and ii) what is their evolution upon loading from the in-situ stress state and subsequent unloading.

The model in Figure 15 shows that the oriented *scales* that characterise the SCM scaly clay generate two dominant pore classes, P1 and P3, associated with intra-scale pores (nanometre size) and inter-*scale* pores (from 100 μm to several mm), respectively. These two classes are always present in the (natural) scaly clay, regardless the clay OCR. An intermediate class of pores in the micron range (P2) is generated by curled sub-parallel particles forming rounded pores. This class is only recorded in the overconsolidated state (Figure 9c-e), as further exploited in the evolutionary model in Figure 16. P2 is associated with inter-particle porosity as this class is the only one that is observed in reconstituted clay, where Fearon and Coop (2000) and Vitone and Cotecchia (2011) provided evidence that the scaly structure is fully erased by the remoulding at high water content. the reconstituted clay shows higher 'interlocking' compared to oriented *scales* and particles in the natural clay (Figure 15).

The evolutionary framework presented in Figure 16 provides a more comprehensive interpretation of the mechanisms inferred by Vitone et al. (2018) on the basis of just SEM photographs of scaly clays. The authors suggested that loading of scaly clays along the NCL causes two simultaneous and 'opposite' processes in terms of their effect on the global response of the clay: 1) the closure of the fissures between the *scales* and 2) the degradation of the *scales.*

With respect to point 1), Figure 16 shows that plastic deformation upon loading occurs with a non-reversible transfer of porosity from class P3 to class P1 (see item i) in section 4.2.3). The mechanism associated with this process would consist in the permanent closing up of the inter-*scale* porosity, with the generation of new intra-*scale* porosity P1 (Figure 16a).

Porosity P2 is instead likely the main contributor to point 2). Its disappearance when the clay is brought to a NC state (see item ii) in section 4.2.3) is seen via SEM photographs to be associated with the flattening and rebounding of curled particles (Figure 16b). This is the same mechanism expected to control elastic response of reconstituted clays (having only P2).

The 'curling' of clay particles would also explain the P2 rebound when the natural clay is unloaded from the in-situ stress state (see item iii) in section 4.2.3). This is likely addressing the third main research question of this study, i.e., about the similarity observed among the slope of the loading-unloading curves of the natural clay and the reconstituted.

Unloading from the normally consolidated state (6800 kPa) generates an increase in porosity P3 in part compensated by a decrease in porosity P1 (see item iv) in section 4.2.3). A minor part of the porosity transferred from P3 to P1 upon loading (closure of inter-*scale* porosity) appears to be transferred in reverse direction upon unloading (Figure 16c).

CONCLUSIONS

This paper has presented a microstructural study on an Italian intensely fissured (scaly) clay that has been chosen as representative of many others, widely outcropping in chain areas (e.g., AGI 1979, 1985; Vannucchi et al., 2003), with such intensely fissured structure, high plasticity and activity. Intensely fissured clays have been widely studied due to their very low strength and high swelling capacity which make them responsible for severe and unexpected problems in situ. The research has been conducted by measuring the evolution of pore-size distribution upon mechanical loading and unloading via the unique combination of Mercury Intrusion Porosimetry (MIP) and X-ray Computed Tomography (XCT). This investigation was complemented by the observation of SEM images.

The microstructural study was aimed at elucidating some complex and non-intuitive aspects of compression behaviour of scaly clays. Three research questions were addressed, i) which pore classes are involved in the volumetric response of the clay; ii) how they evolve upon loading and unloading; iii) why the slope of the loading-unloading curve of the natural clay is very similar to the slope of the unloading curve of the same clay in reconstituted state.

Scaly clays appear to be characterised by three pore classes, the smaller one associated with intra-*scale* porosity and the larger one associate with inter-*scale* porosity. The intermediate pore-class was associated with the porosity between non-aggregated particles, as this class overlaps with the porosity class present in the reconstituted clay (where *scales* are destroyed by remoulding the clay at high water content).

Inter-*scale* porosity appears to be the main driver of plastic compression; inter-*scale* porosity converts into intra-*scale* porosity irreversibly when the clay is brought to normal compression states. 'Reversible' response appears to be controlled mainly by the reversible curling and flattening of the particles forming the intermediate class of inter-particle pores. This class is

the only class of pores in reconstituted clay, thus explaining why unloading curves of the natural scaly clay is astonishingly parallel the unloading curve of the same clay in reconstituted state.

Another peculiar aspect of the compression behaviour of scaly clays is associated with the very similar slope of the loading and unloading curves compared with the very different slope of normal compression and unloading curves of the same clay in reconstituted clay. At the same time, normal compressibility of the natural clay is much lower than that of reconstituted clay. This different response is associated with the pore class driving the transition from normally to overconsolidated states. In reconstituted clays, plastic compression is associated with the suppression of large pores belonging to a mono-modal PSD. For scaly clays, transition from overconsolidated to normally consolidated states is controlled by the suppression of inter-*scale* porosity. However, this porosity does not disappear and is partially converted into intra-*scale* porosity. At macroscopic scale, the suppression of inter-*scale* porosity is therefore barely noticeable.

References

Bilotta, E., Pellegrino, A. & Picarelli, L. 1985. Geotechnical properties and slope stability in structurally complex clay soils. Chapter 3: Physical and mechanical properties. *Geotechnical Engineering in Italy. An overview, 1985.* Associazione Geotecnica Italiana.

Burland, J. 1990. On the compressibility and shear strength of natural clays. *Geotechnique,* 40, 329-378.

Cicolella, A. & Picarelli, L. 1990. Decadimento meccanico di una tipica argilla a scaglie di elevata plasticita. *Rivista Italiana di Geotecnica,* 24, 5-23.

Cotecchia, F. & Vitone, C. On the model requirements to predict the behaviour of fissured clays. Proceedings of the 15th European Conference on Soil Mechanics and Geotechnical Engineering, 2011. IOS Press, 525-530.

Cotecchia, F., Vitone, C., Santaloia, F., Pedone, G. & Bottiglieri, O. 2015. Slope instability processes in intensely fissured clays: case histories in the Southern Apennines. *Landslides,* 12, 877-893.

Cotecchia, V. & Valentini, G. 1973. Comportamento Allo Scavo In Galleria Di Rocce Argillose Tipiche Dell'appennino Meridionale.

Di Maio, C. 1996. Exposure of bentonite to salt solution: osmotic and mechanical effects. *Geotechnique,* 46, 695-707.

Diamond, S. 1970. Microstructure and pore structure of impacted-compacted clays. *Clays Clay Miner,* 19, 239-249

Fearon, R. & Coop, M. 2000. Reconstitution: what makes an appropriate reference material? *Géotechnique,* 50, 471-477.

Fearon, R. & Coop, M. 2002. The influence of landsliding on the behaviour of a structurally complex clay. *Quarterly journal of engineering geology and hydrogeology,* 35, 25-32.

Gens, A. On the hydromechanical behaviour of argillaceous hard soils-weak rocks. Proceedings of the 15th European Conference on Soil Mechanics and Geotechnical Engineering–Geotechnics of Hard Soils–Weak Rocks (Part 4). A. Anagnostopoulos et al.(Eds.). IOS Press, 2013. 71-118.

Leroueil, S. & Vaughan, P. 1990. The general and congruent effects of structure in natural soils and weak rocks. *Géotechnique,* 40, 467-488.

Melidoro, A., Melidoro, G. & Panaro, V. 2002. Deformazioni gravitative dei versanti nei terreni flisciodi con argille a bentoniti di Santa Croce di Magliano (Molise). *Quarry & Construction,* 2, 11-17.

Münch, B. & Holzer, L. 2008. Contradicting geometrical concepts in pore size analysis attained with electron microscopy and mercury intrusion. *Journal of the American Ceramic Society,* 91, 4059-4067.

Murray, I. & Tarantino, A. 2019. Mechanisms of failure in saturated and unsaturated clayey geomaterials subjected to (total) tensile stress. *Géotechnique,* 69, 701-712.

Nardelli, V., Coop, M., Vitone, C. & Chen, S. 2016. The inter-scale behaviour of two natural scaly clays. *Géotechnique letters,* 6, 205-210.

Pechalat, M., Chambon, M., Lebrun, M., Tincelin, T., Comes, M., Cordel, C., Marin, M., Fourmaintreaux, M., Louis, M. & Raffoux, J. Some Italian Experiences On The Mechanical Characterization Of Structurally Complex Formations. ISRM Congress, 1979. ISRM, ISRM-4CONGRESS-1979-110.

Pedrotti, M. 2016. *An experimental investigation on the micromechanics of non-active clays in saturated and partially-saturated states.* Ph.D. Thesis, University of Strathclyde, Glasgow, Scotland, UK.

Pedrotti, M. & Tarantino, A. 2018. An experimental investigation into the micromechanics of non-active clays. *Géotechnique*, 1-18.

Picarelli, L., Olivares, L., Di Maio, C., Silvestri, F., Di Nocera, S. & Urciuoli, G. 2003. Structure properties and mechanical behaviour of the highly plastic intensely fissured Bisaccia clay shale. *Characterisation and engineering properties of Natural Soils, AA Balkema, Lisse, the Netherlands,* 2, 947-982.

Santaloia, F., Cotecchia, F. & Polemio, M. 2001. Mechanics of a tectonized soil slope: influence of boundary conditions and rainfall. *Quarterly journal of engineering geology and hydrogeology,* 34, 165-185.

Schindelin, J., Arganda-Carreras, I., Frise, E., Kaynig, V., Longair, M., Pietzsch, T., Preibisch, S., Rueden, C., Saalfeld, S. & Schmid, B. 2012. Fiji: an open-source platform for biological-image analysis. *Nature methods,* 9, 676-682.

Schofield, A. & Wroth, P. 1968. *Critical state soil mechanics*, McGraw-Hill London.

Silvestri, F., Vitone, C., D'onofrio, A., Cotecchia, F., Puglia, R. & De Magistris, F. 2007. The influence of meso-structure on the mechanical behaviour of a marly clay from low to high strains. *Soil Stress-Strain Behavior: Measurement, Modeling and Analysis.* Springer.

Soil, A. C. D.-O. & Rock 2017. *Standard Practice for Classification of Soils for Engineering Purposes (Unified Soil Classification System) 1*, ASTM international.

Sridharan, A. & Venkatappa Rao, G. 1973. Mechanisms controlling volume change of saturated clays and the role of the effective stress concept. *Geotechnique,* 23, 359-382.

Tarantino, A., Sacchet, A., Dal Maschio, R. & Francescon, F. 2010. A Hydromechanical Approach to Model Shrinkage of Air-Dried Green Bodies. *Journal of the American Ceramic Society,* 93, 662-670.

TAR , G. & Ferreira, J. M. 1998. Influence of solid loading on drying-shrinkage behaviour of slip cast bodies. *Journal of the European Ceramic Society,* 18, 487-493.

TAR , G., Ferreira, J. M. & Fonseca, A. T. 1999. Influence of particle size and particle size distribution on drying-shrinkage behaviour of alumina slip cast bodies. *Ceramics International,* 25, 577-580.

Vannucchi, P., Maltman, A., Bettelli, G. & Clennell, B. 2003. On the nature of scaly fabric and scaly clay. *Journal of Structural Geology,* 25, 673-688.

Vesga, L. F. 2009. Direct tensile-shear test (DTS) on unsaturated kaolinite clay.

Vitone, C. & Cotecchia, F. 2011. The influence of intense fissuring on the mechanical behaviour of clays. *Géotechnique,* 61, 1003-1018.

Vitone, C., Cotecchia, F., Federico, A. & Viggiani, G. 2018. On the geomechanical characterisation of complexities in clays: experimental studies. *Riv. Ital. Geotec,* 2, 1-29.

Vitone, C., Cotecchia, F., Viggiani, G. & Hall, S. 2013. Strain fields and mechanical response of a highly to medium fissured bentonite clay. *International Journal for Numerical and Analytical Methods in Geomechanics,* 37, 1510-1534.

Table 1. fissuring characterization, composition, plasticity properties and mineralogy of the SCM scaly clay. Key: F-ID: fissuring identity; CF: clay fraction; MF: silt fraction; SF: sand fraction; PI: plasticity index; w_L: liquid limit; γ_s: soil solid unit weight; A: activity index; * in the fraction < 2μm; I/S: mixed-layers illite/smectite (percentage of illite is specified in brackets); I: illite; K: kaolinite; Ch: chlorite.

Main F-ID	CF [%]	MF [%]	SF [%]	PI [-]	w_L [%]	A [-]	γ_s [kN/m^3]	USCS classification	Mineralogical composition*			
									I/S	I	K	Ch
F1-I6	83	16	1	0.59	99	0.7	27.12	CH	80 (30-35)	2	16	2

Table 2. Specimens subjected to micro-structural investigation

	Test ID	Sample type	$\sigma'_{constant\ volume}$	σ'_{max} [kPa]	σ'_{final}[kPa]	Suction [kPa]	MIP	X-CT	SEM
1D compression	OED1	Natural	400	6400	6400	-	x	x	x
	OED2		350	350	50	-	x	x	x
	OED3		400	6400	400	-	x	x	-
	OED4		400	400	400	-	x	x	x
	OED5		400	1200	1200	-	-	-	-
	OED1*	Reconstituted	-	6400	6400	-			
	OED2*		-	4900	300	-	-	-	-
Isotropic drying	N	Natural	-	-	-	323	x	-	x
	N-s9000		-	-	-	9000	x	-	-
	Recon-s400	Reconstituted	-	-	-	400	x	-	-
	Recon-s1400		-	-	-	1400	x	-	-
	Recon-s2800		-	-	-	2800	x	-	x

Figure captions

Figure 1. Normalized 1D compression curves. (natural and reconstituted SCM scaly clay vs. (natural and reconstituted high-smectite content clays

Figure 2. Natural scaly clay under study (Santa Croce di Magliano - SCM, Italy).

Figure 3. Specimens subjected to microstructural investigation. (a) One-dimensional compression tests (b) Isotropic compression through air drying-induced suction

Figure 4. Qualitative comparison between input image (a) and distance map of the pore space (b). In the input image, dark areas correspond to void space, whereas brighter areas to solid space. In the distance map, white areas correspond to solid space and coloured areas to void space. Within the void space brighter areas (yellow) correspond to larger pores and darker areas (blue) to smaller pores.

Figure 5. 'Realignment' of the pore-size distributions derived from MIP and XCT image analysis (specimen OED1)

Figure 6. Oedometer tests on natural and reconstituted SCM scaly clay.

Figure 7. Suction-induced compression for natural state and reconstituted samples. Desiccation data are compared to oedometer curve on sample reconstituted from slurry showed in Figure 6. Arrows indicate name of the samples where MIP was performed.

Figure 8. Cumulative pore size distributions of natural scaly clay specimens subjected to 1D loading or unloading (pore size distribution obtained by joining MIP and X-CT data).

Figure 9. Frequency pore size distributions of natural scaly clay specimens subjected to 1D loading or unloading (pore size distribution obtained by joining MIP and X-CT data). a) specimen OED2 (50 kPa), b) specimen OED4 (400 kPa), c) specimen OED5 (1200 kPa), d) specimen OED1 (6400 kPa), e) specimen OED3 (400 kPa).

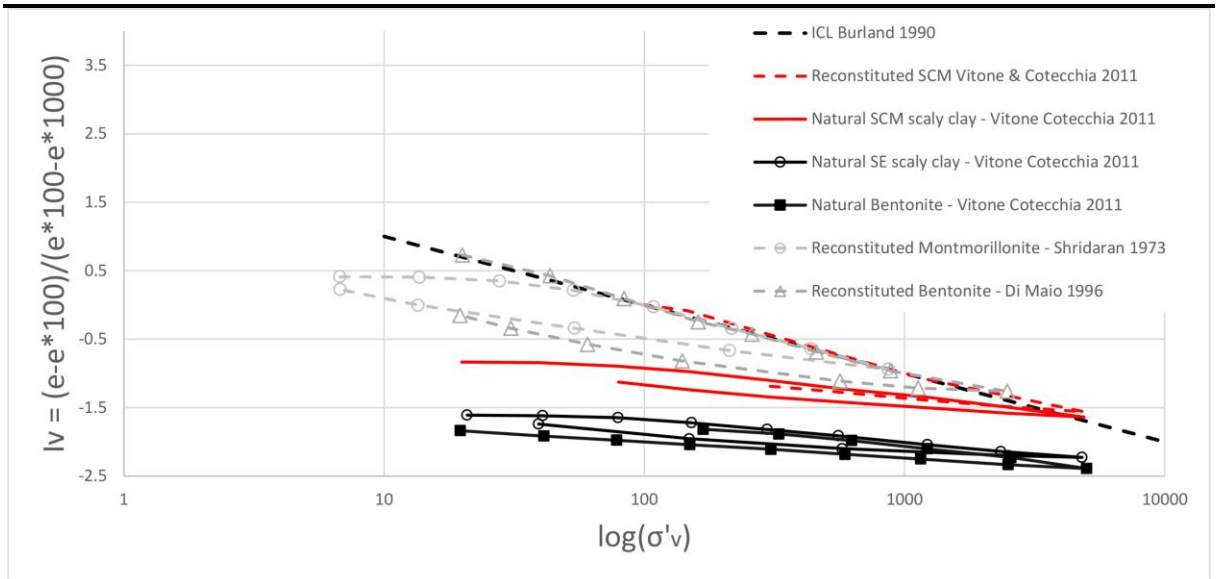

Figure 1

Figure2

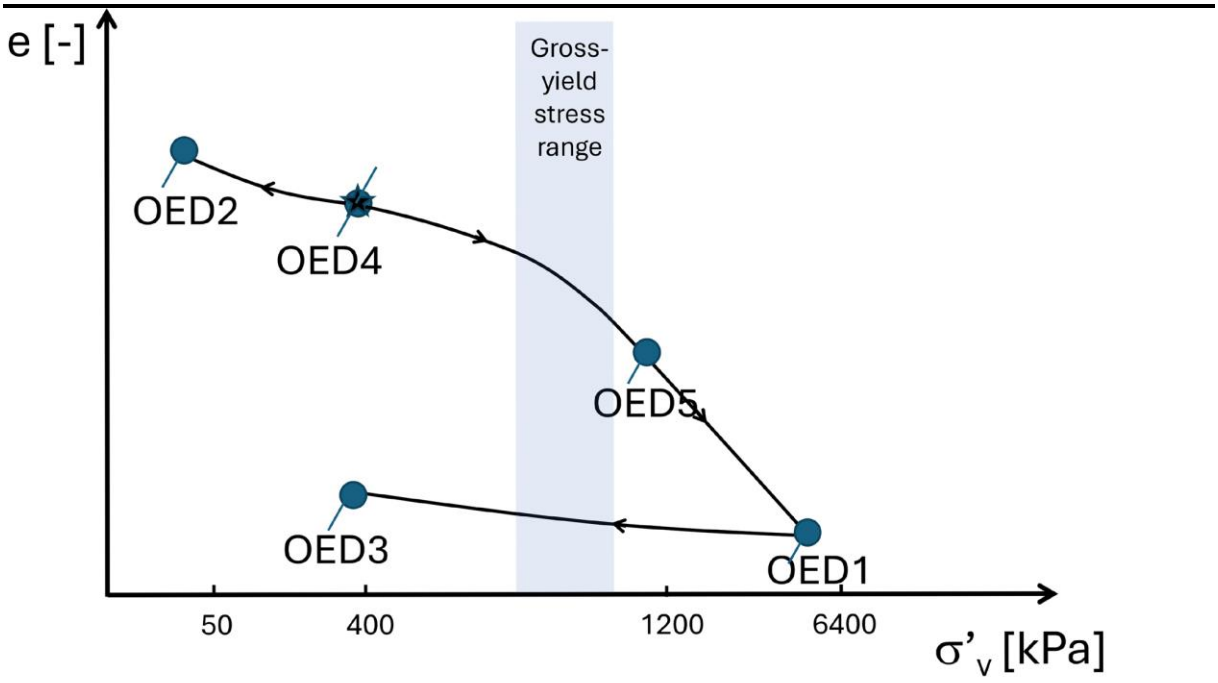

Figure3a

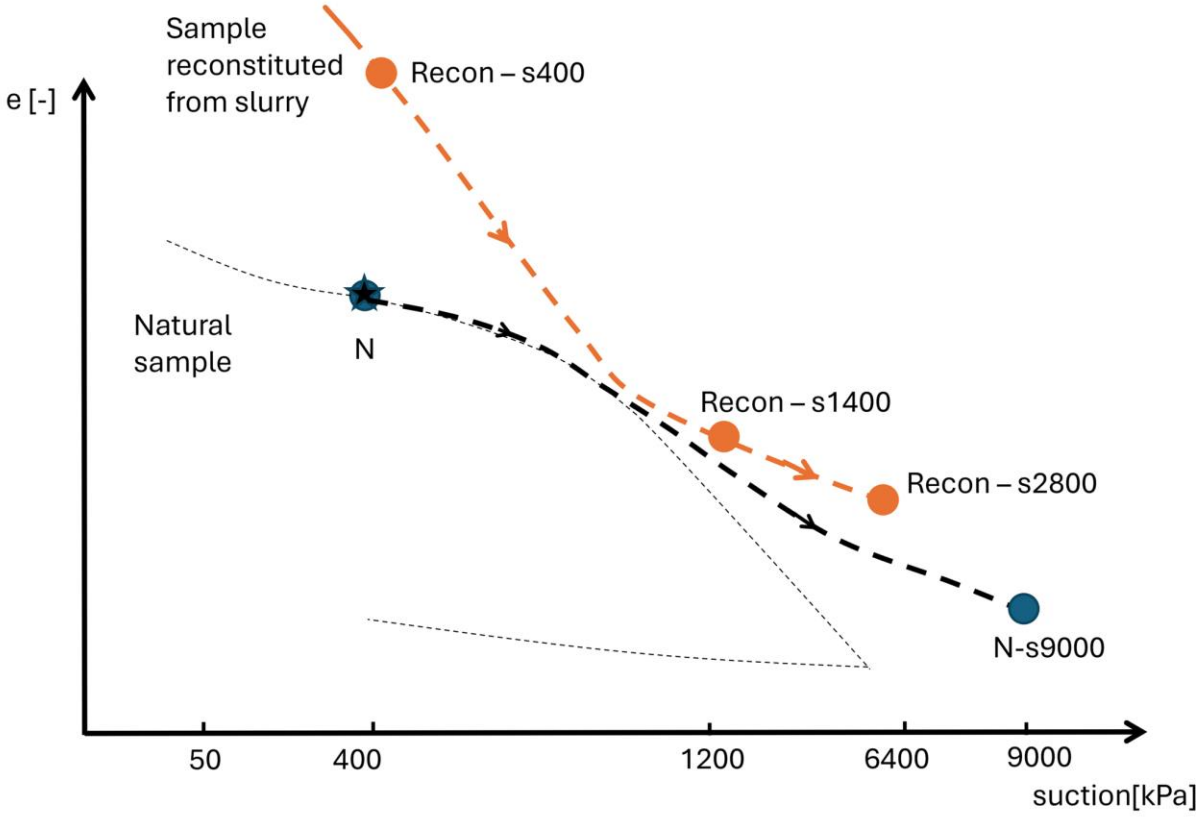

Figure3b

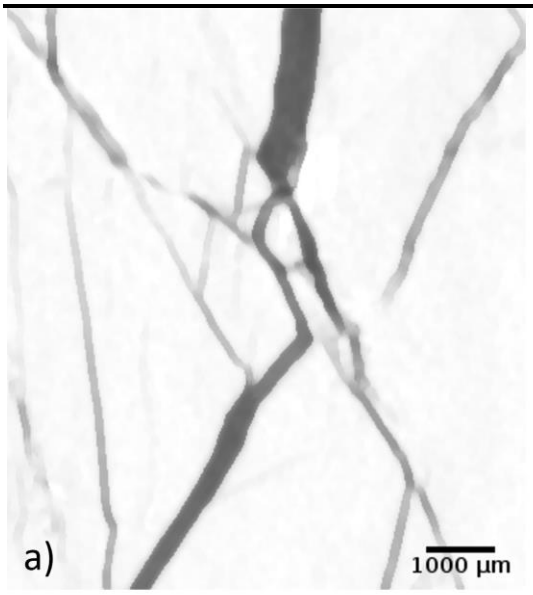

Figure4a

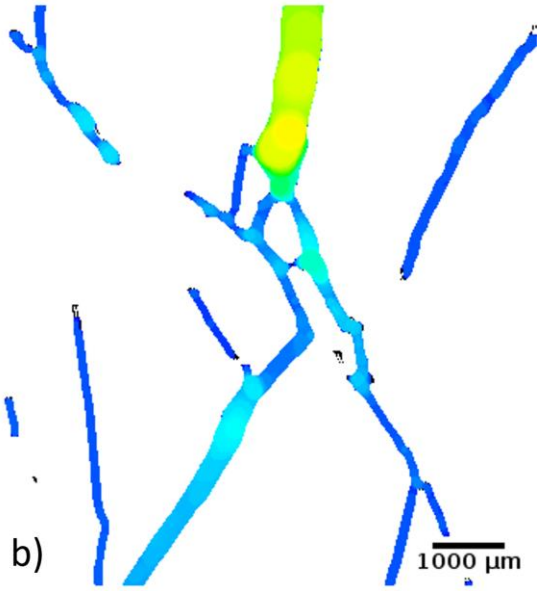

Figure4b

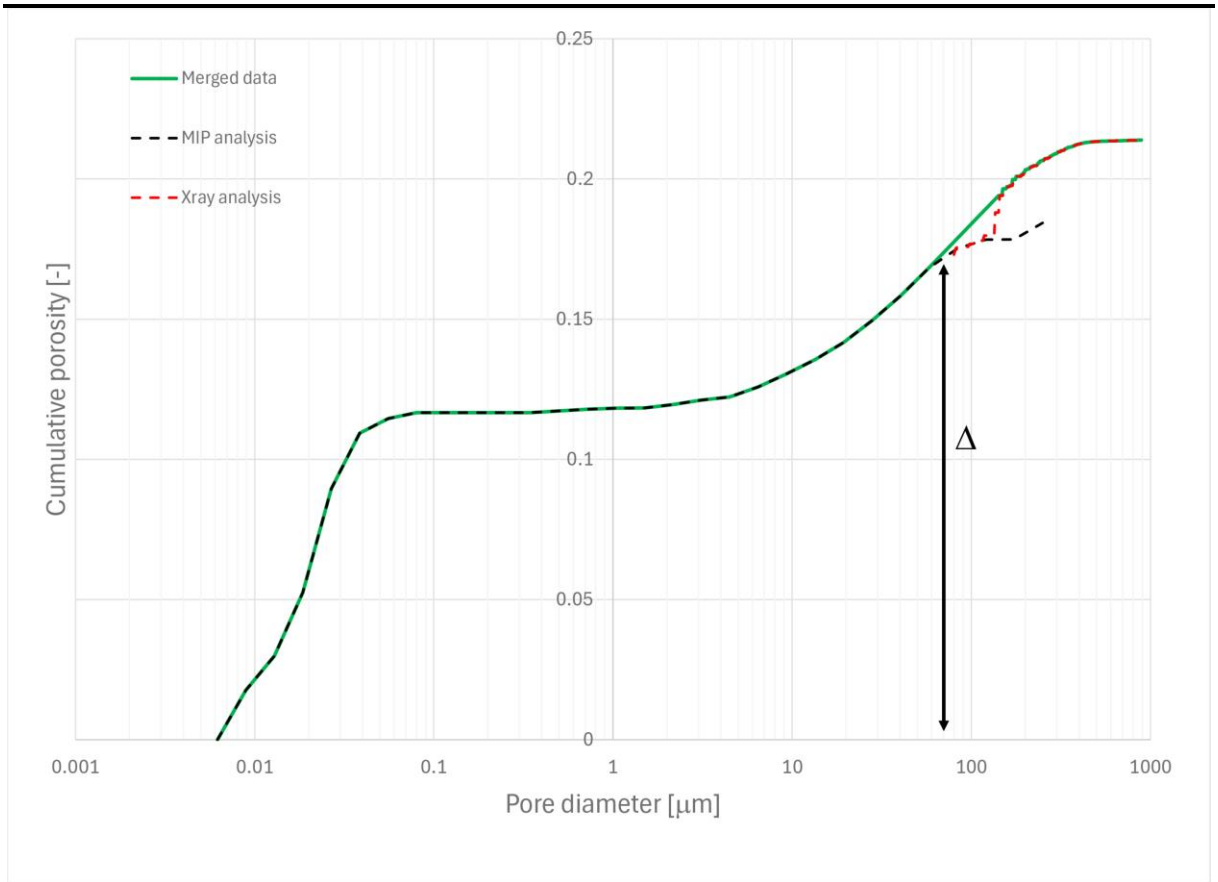

Figure 5

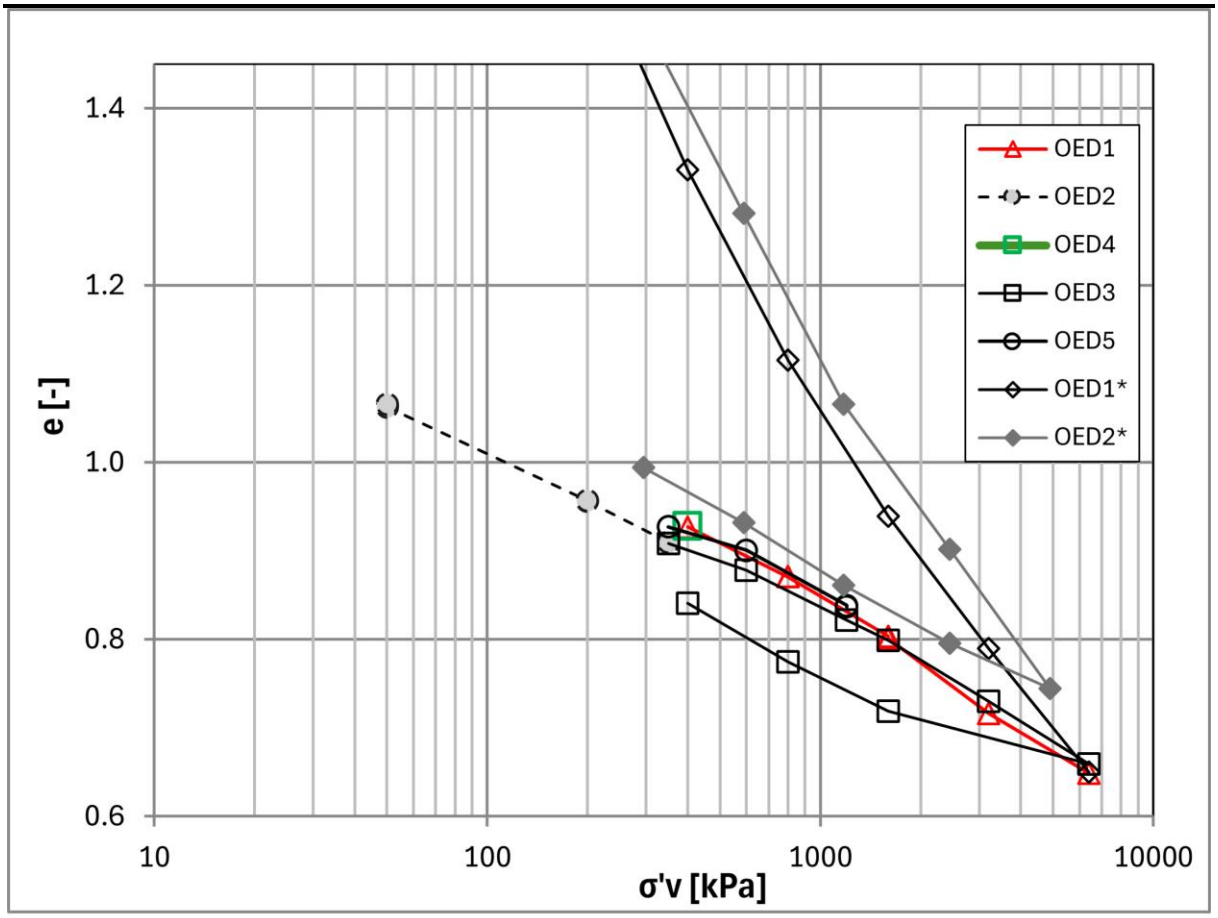

figure6

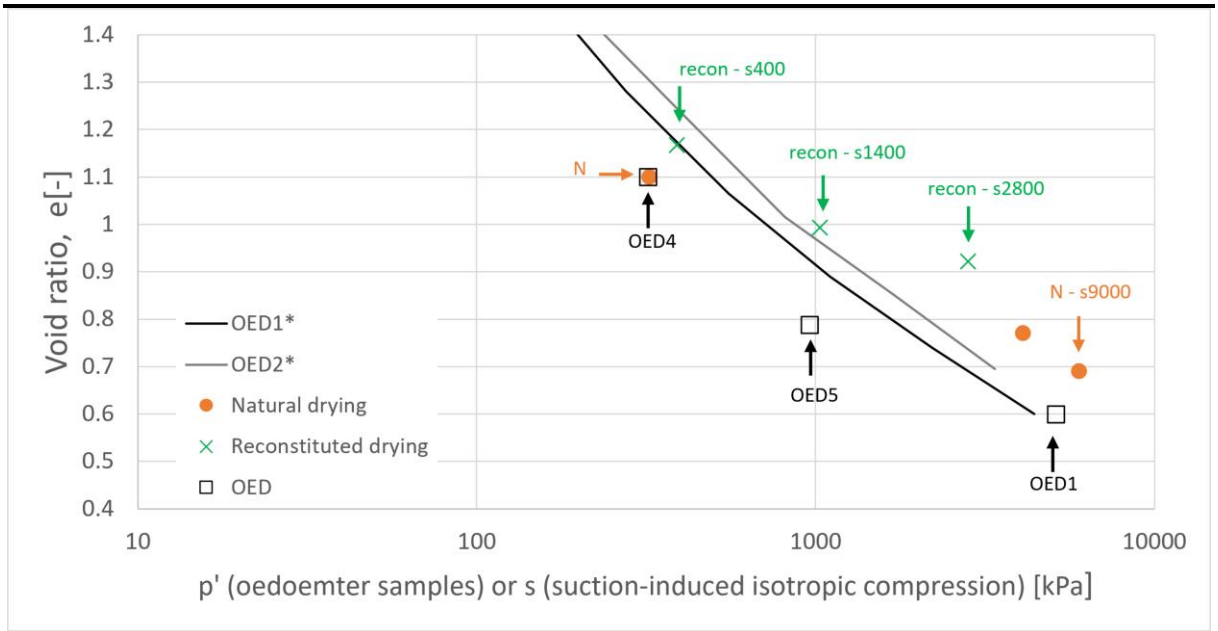

Figure7

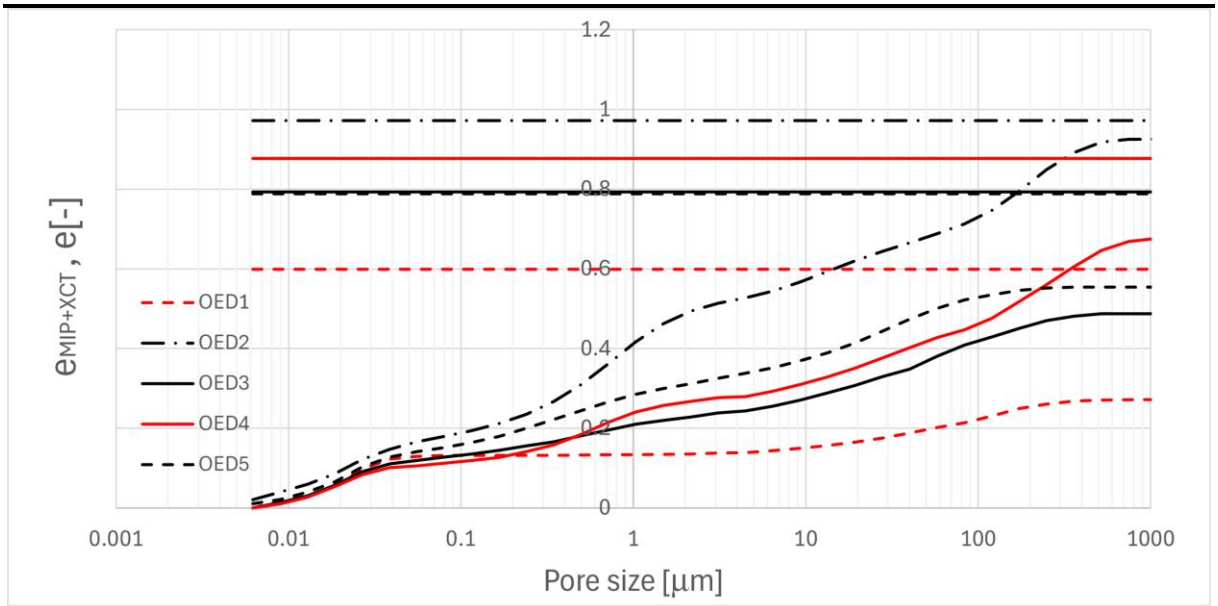

figure8

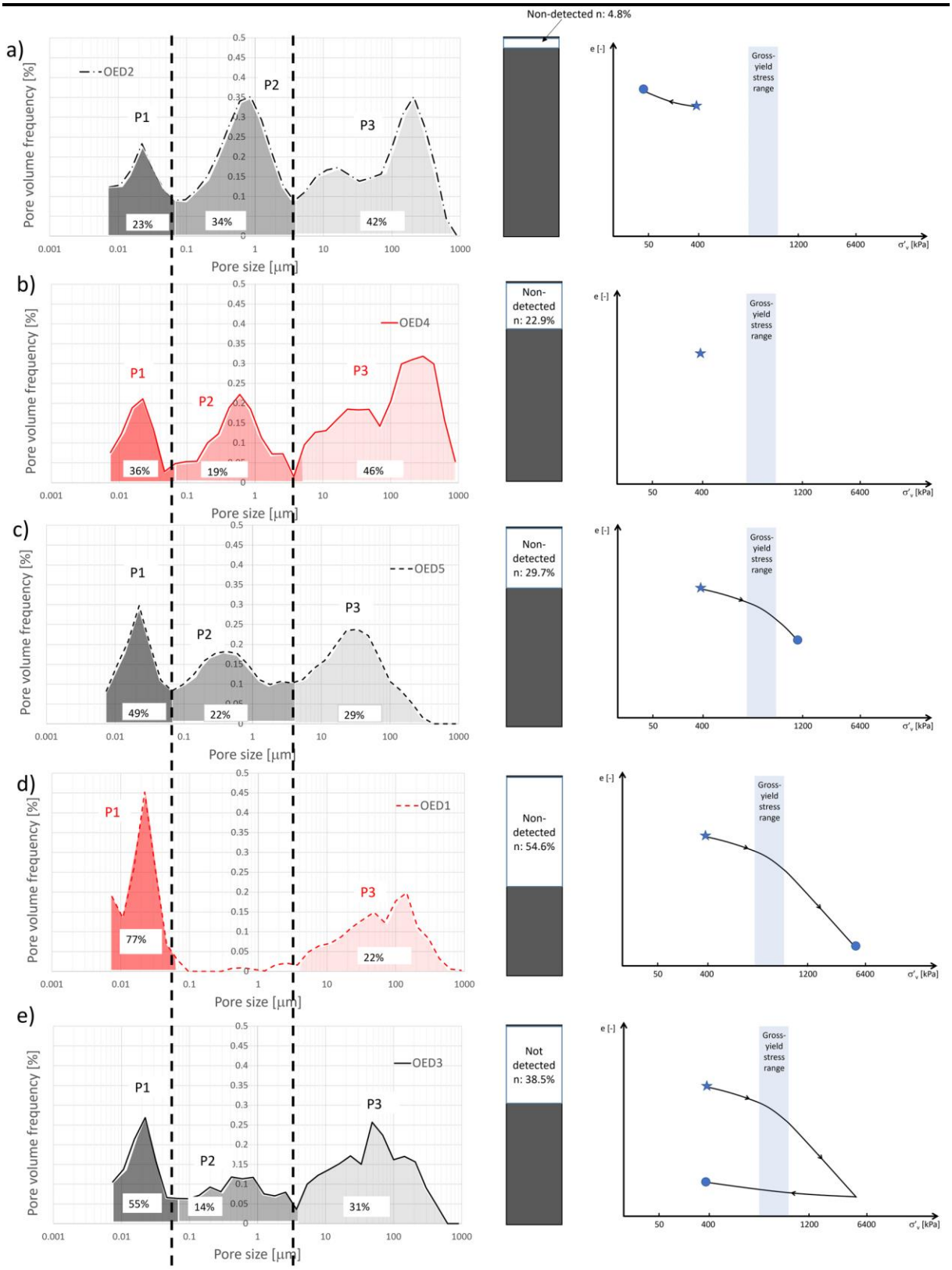

Figure9

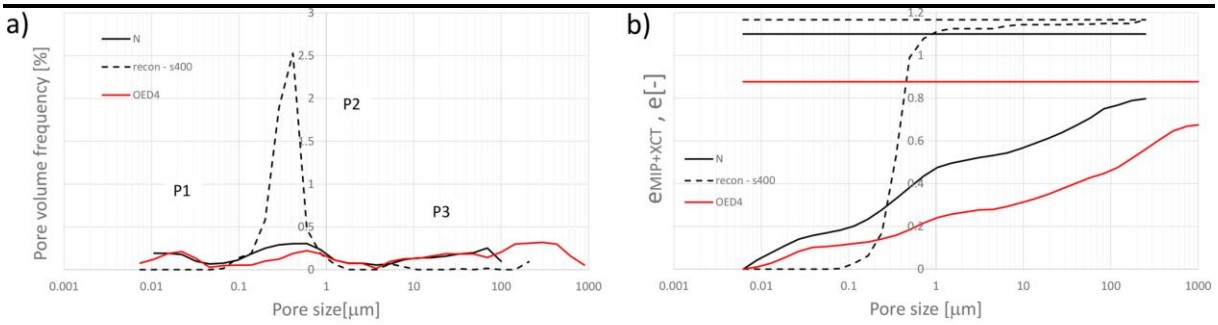

Figure 10

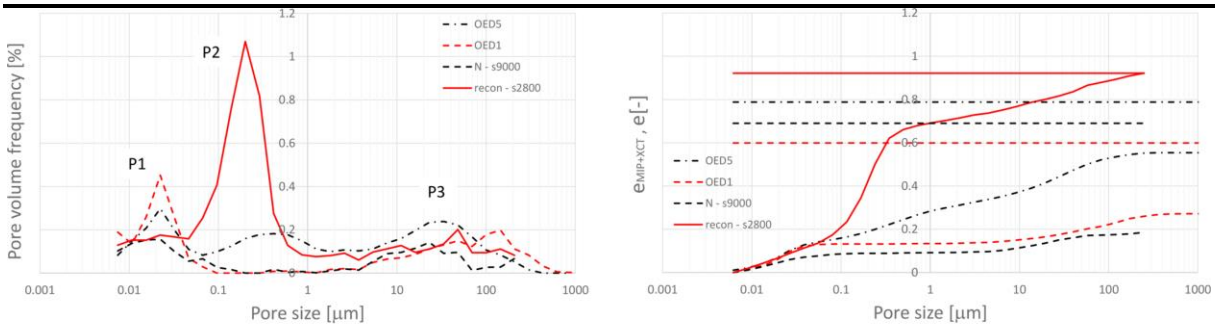

Figure 11

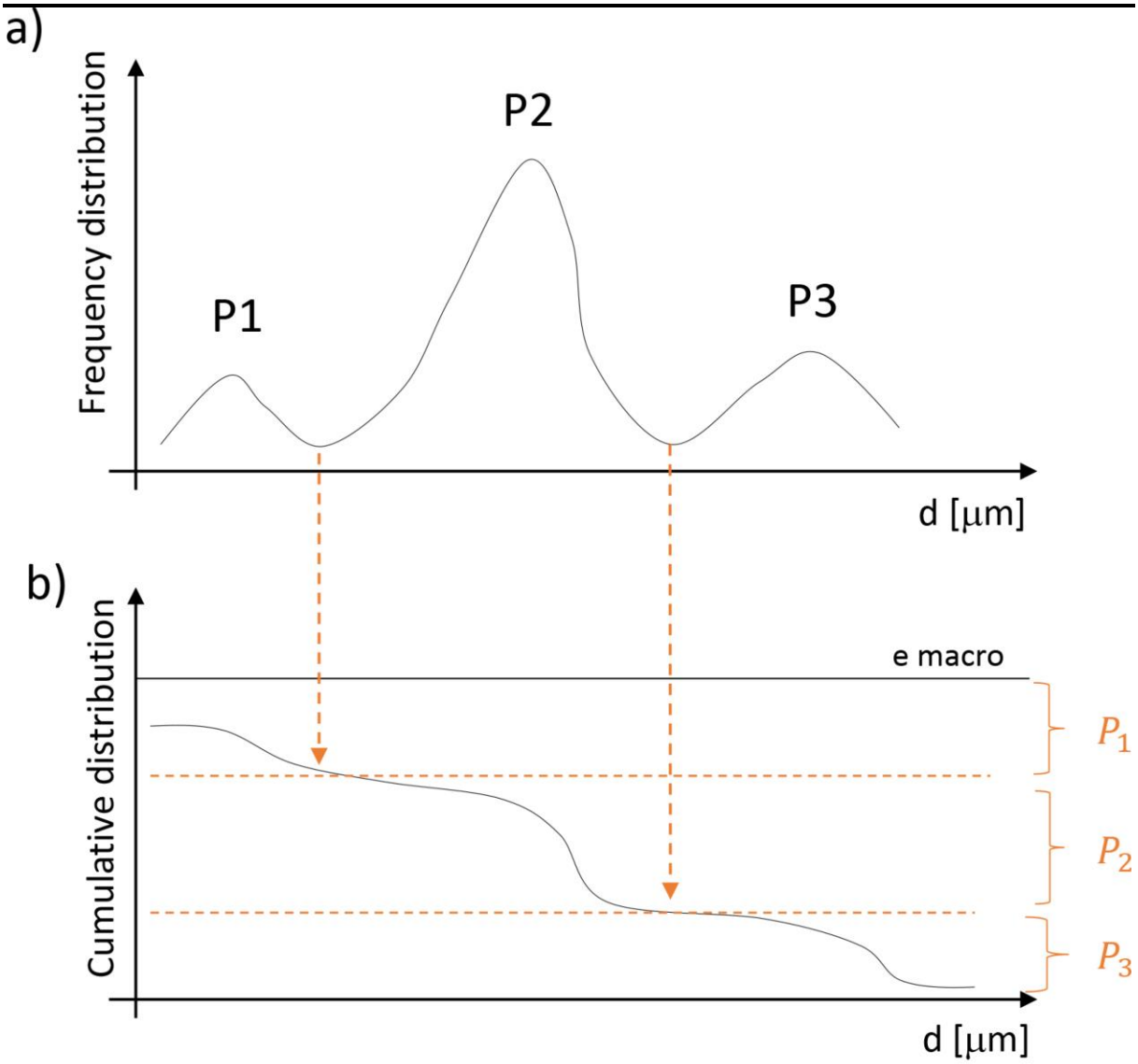

Figure 12

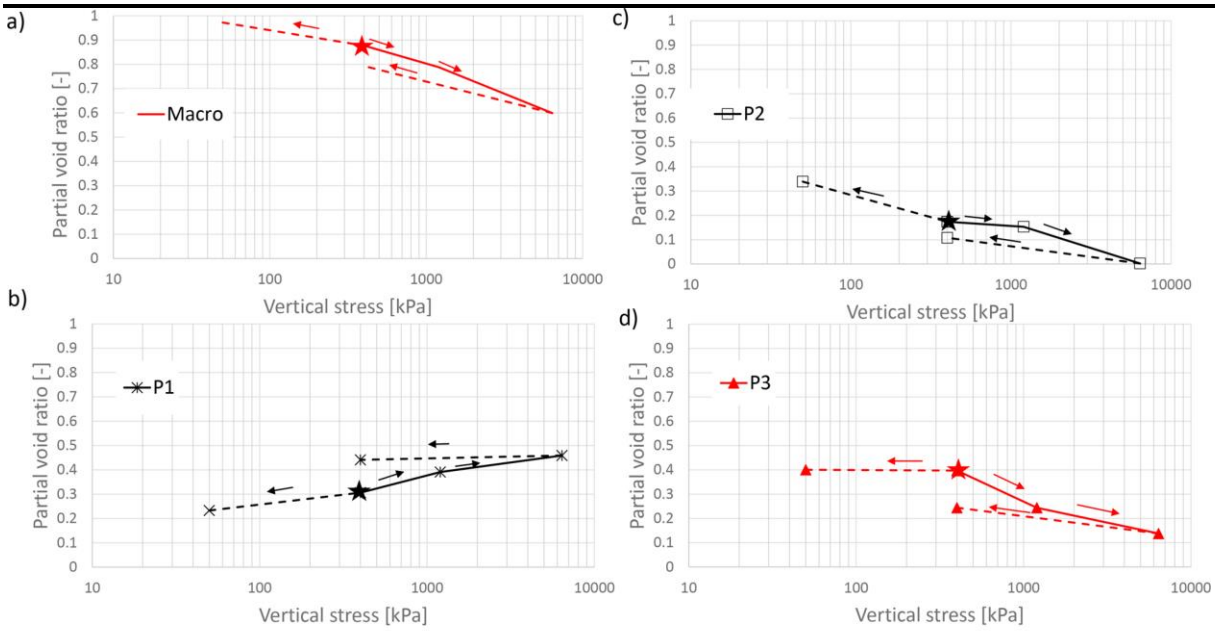

Figure 13

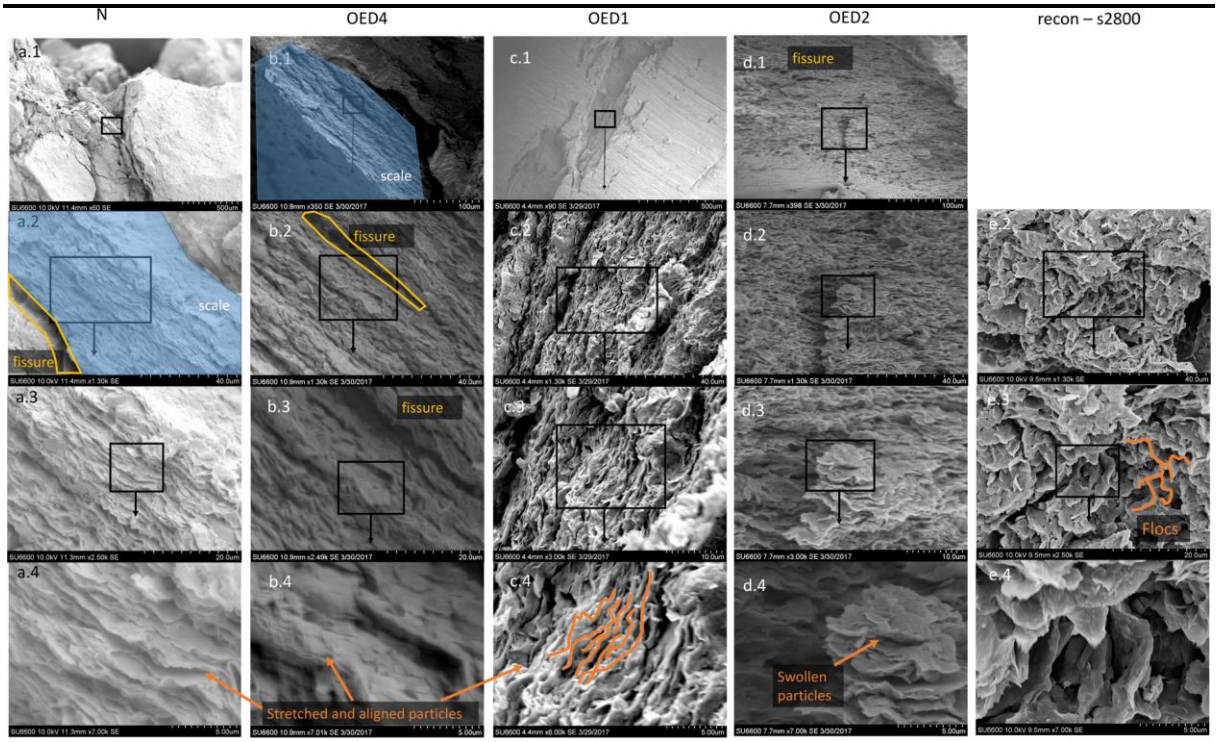

figure14

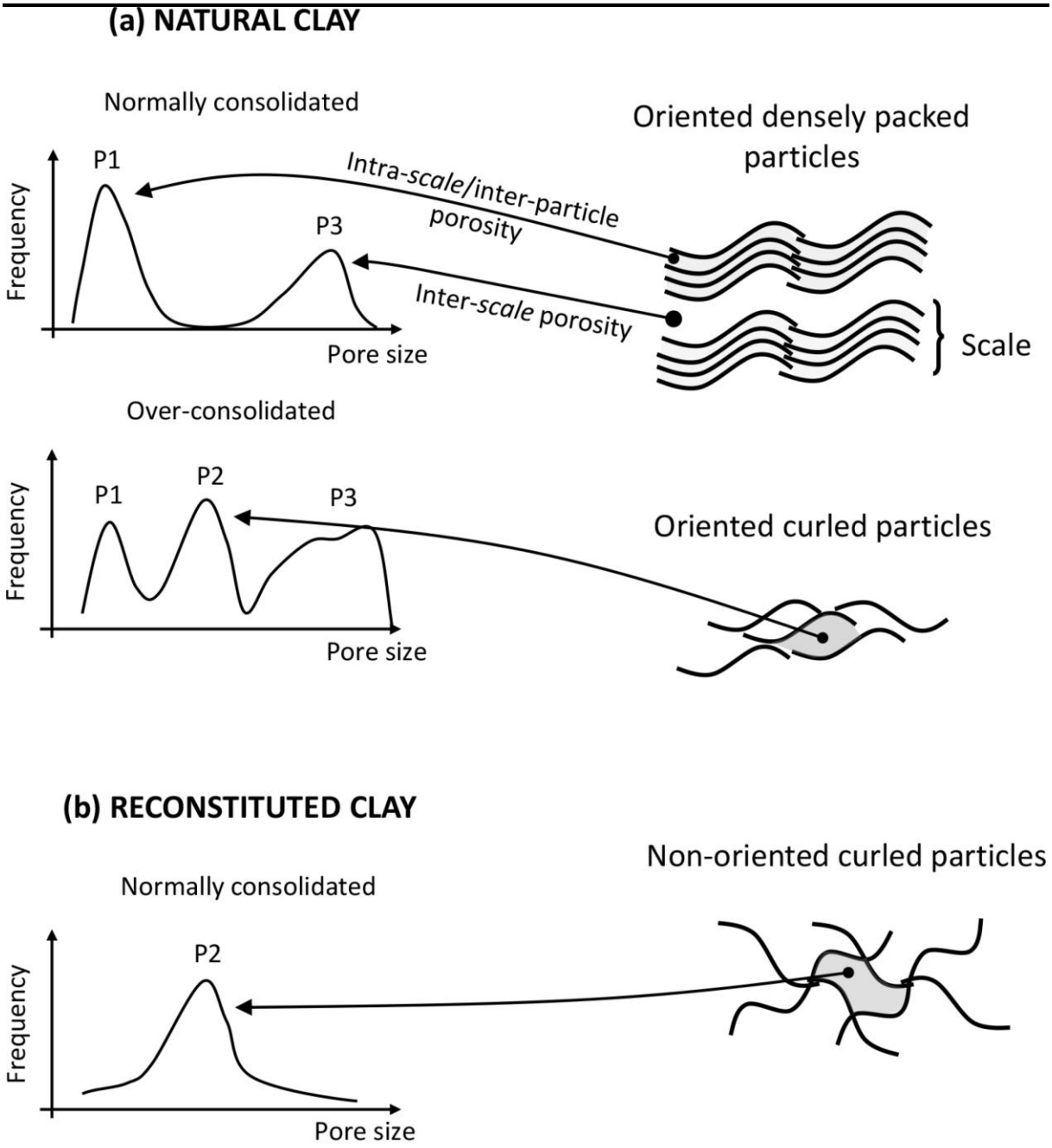

figure15

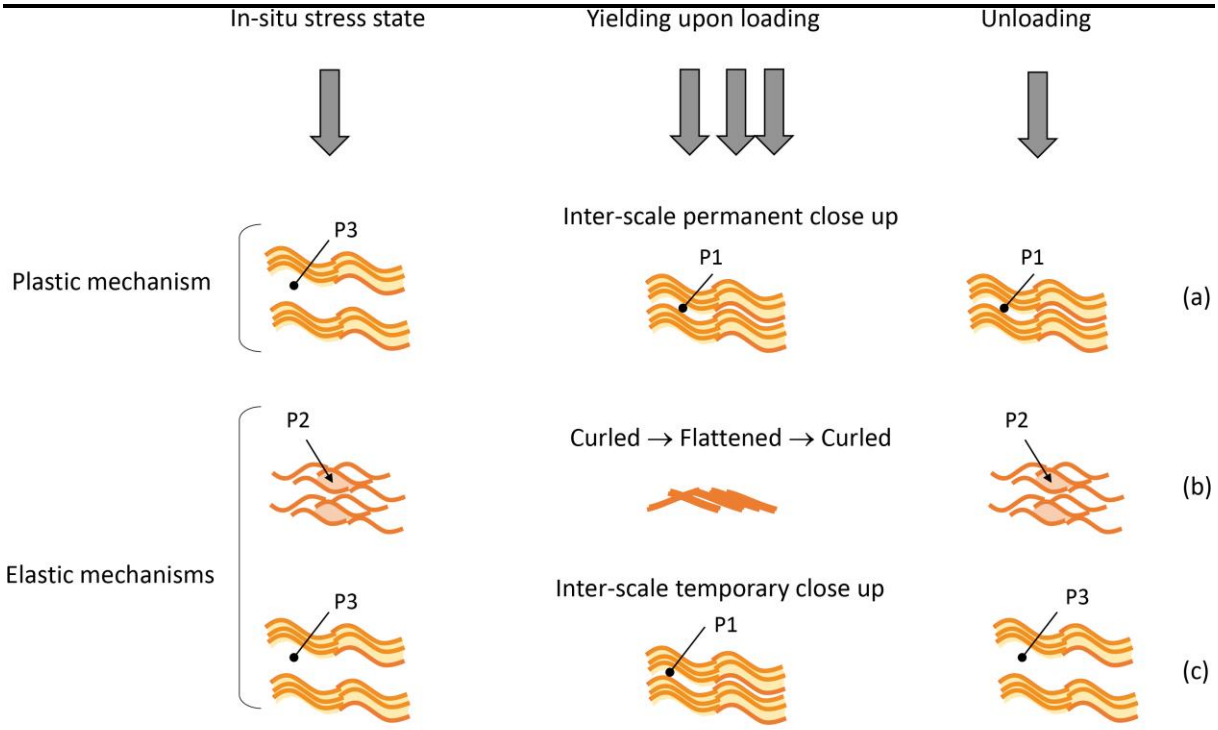

figure16